Structurally flexible pyrrolidinium- and morpholinium-based ionic liquid electrolytes

(article starts on next page)

Structurally flexible pyrrolidinium- and morpholinium-based ionic liquid electrolytes†

Sourav Bhowmick, [ID] [a] Gaurav Tatrari, [ID] [a] Andrei Filippov, [ID] [a] Patrik Johansson [ID] *[bc] and Faiz Ullah Shah [ID] *[a]

Ion transport measures and details as well as physico-chemical and electrochemical properties are presented for a small set of structurally flexible pyrrolidinium (Pyrr) and morpholinium (Morph) cation-based ionic liquids (ILs), all with oligoether phosphate-based anions. All have high thermal stabilities, low glass transition temperatures, and wide electrochemical stability windows, but rather moderate ionic conductivities, where both the anions and the cations of the Pyrr-based ILs diffuse faster than those of the Morph-based ILs. Overall, the Pyrr-based ILs show significantly more promise as high-temperature supercapacitor electrolytes, rendering a specific capacitance of 164 F g^{-1} at 1 mV s^{-1}, a power density of 609 W kg^{-1} and a specific energy density of 27 W h kg^{-1} at 90 °C in a symmetric graphite supercapacitor.

Introduction

In the past decades, ionic liquids (ILs) have demonstrated promising performance characteristics in a range of exciting potential applications, such as solvents,[1] electrolytes for different energy storage devices,[2] catalysts,[3] lubricants,[4] extractants,[5] absorbents,[6] magnetic fluids,[7] optical fluids,[8] crystallization media,[9] and antibacterial media for biomedical devices.[10] The main reasons for their use are their negligible vapor pressures, large liquidus ranges, high thermal stabilities, non-flammable properties with wide electrochemical stability windows (ESWs), and great potential in structural designability compared with organic solvents.[11,12]

From the point of view of the IL cation structural designability, N-heterocycles such as pyrrolidinium (Pyrr) and morpholinium (Morph) rings are very interesting synthons for the development of new task-specific ILs due to their small and compact sizes.[13] These rings can be ionized upon quaternization of the tertiary nitrogen atom, resulting in a stable positive charge.[14] Furthermore, the oxygen atom in the Morph ring widens the ESW and enhances the ionic conductivity.[15] In comparison with other ILs, both Pyrr- and Morph-based ILs show higher ionic conductivities, wider ESWs, higher thermal stabilities, and lower viscosities.[15,16] In addition, they are less toxic and more biodegradable than conventional ILs based on other cations.[17–19]

Turning to the design of IL anions, interest in alkyl phosphate-based anions is growing, not least due to safety concerns regarding energy storage devices, where the anions play a key role in the optimization of separator[20] and electrode materials,[21] and are used as electrolyte additives for overcharge protectors and redox mediators.[22,23] With respect to the latter, the most common flame retardants are organophosphorus organic compounds[24–27] or ILs;[28,29] the former compounds, however, are limited by their lower ESWs and thermal stabilities, which is why ILs with phosphate-based anions are promising.

Here, ILs based on oligoether phosphate-based anions and Pyrr- and Morph-based cations, with different oligoether chain lengths are synthesized and subsequently studied with respect to their physico-chemical and electrochemical properties alongside their ion transport properties, with the overall aim of being used as (high-temperature) electrolytes with high ionic conductivities, wide ESWs, and low glass transition temperatures.

Experimental

Materials, synthesis and characterisation

Phosphorus(v) oxychloride (99% purity; Sigma Aldrich), diethylene glycol ethyl ether (99% purity; Sigma Aldrich), triethylene glycol monomethyl ether (95% purity; Sigma Aldrich), 1-methylpyrrolidine (98% purity; Sigma Aldrich) and 4-methylmorpholine (99% purity; Sigma Aldrich), sodium sulfate (99% purity; Sigma Aldrich), ethyl acetate (99.5% purity; Sigma Aldrich) and hexane (99% purity;

a Chemistry of Interfaces, Lulea University of Technology, SE-971 87 Lulea, Sweden. E-mail: faiz.ullah@ltu.se

b Department of Physics, Chalmers University of Technology, SE-412 96 Gothenburg, Sweden. E-mail: patrik.johansson@chalmers.se

c ALISTORE-European Research Institute, CNRS FR 3104, Hub de l'Energie, 80039 Amiens, France

This journal is © the Owner Societies 2023

Phys. Chem. Chem. Phys., 2023, **25**, 19815–19823 | **19815**

Table 1 Molecular weight, water content, glass transition temperature, decomposition temperature, and ionic conductivity values of the ILs

Ionic liquid	MW (g mol^{-1})	Water content (ppm)	T_{decomp} (°C)	T_g (°C)	σ @ 20 °C (mS cm^{-1})
[MmMPyrr][TEEP]	621.70	87 ± 5	238	−76	0.14
[EmMPyrr][DEEP]	531.61	78 ± 5	239	−80	0.10
[MmMMorph][TEEP]	637.70	92 ± 5	224	−69	0.03
[EmMMorph][DEEP]	547.61	74 ± 5	225	−73	0.03

Sigma Aldrich) were used without further purification. The synthesis and characterization details are provided in the ESI.† All of the as-made ILs were kept in a vacuum oven at 90 °C for at least one week until the water content was <100 ppm (Table 1), as determined *via* Karl Fischer titration using a 917 Coulometer (Metrohm) placed inside a glovebox with a water and oxygen content of <1 ppm.

The structure and purity of the intermediate compounds and the final products were confirmed using a nuclear magnetic resonance (NMR) spectrometer with a Bruker Ascend Aeon WB 400 magnet system (Bruker BioSpin AG, Fällanden, Switzerland). CDCl$_3$ was used as a solvent in all the experiments. The working frequencies were 400.21 MHz for ^{1}H, 100.64 MHz for ^{13}C, and 162.01 MHz for ^{31}P. The data were processed using Bruker Topspin 3.5 software. ^{31}P (161.988 MHz) NMR spectra of the ILs as a function of temperature were recorded by placing the sample in a 5 mm standard NMR tube. The sample was heated at 10 K step-wise increments, and measurements were carried out after 15 minutes of thermal equilibration. ESI-MS analysis was performed using a Bruker Impact ESI-Q-TOF system.

Attenuated total reflection Fourier transform infrared (ATR-FTIR) spectra of the intermediate and the final products were recorded using a Bruker IFS 80v spectrometer equipped with a deuterated triglycine sulphate (DTGS) detector and a diamond ATR accessory. The experiments were performed at room temperature ($\sim$20 °C) using the double side forward–backward acquisition mode. 256 scans were co-added and signal-averaged at an optical resolution of 4 cm^{-1}.

Thermal properties

A PerkinElmer 8000 TGA instrument was used for thermogravimetric analysis, which was carried out at a heating rate of 10 °C min^{-1} using nitrogen as the inert carrier gas. A sample of about 3–5 mg was used for each experiment. Pyris software was used to analyse the onset of decomposition temperature (T_{onset}) by taking the intersection of the baseline representing the weight loss and the tangent of the weight *vs.* temperature curve.[30] Differential scanning calorimetry (DSC) was carried out using a PerkinElmer DSC 6000 instrument. About 2–5 mg of sample was packed in an aluminium pan for each experiment. Inert nitrogen gas was used at a constant flow of 20 mL min^{-1}. DSC traces were recorded both during cooling and heating from −135 to 0 °C, with a scanning rate of 5 °C min^{-1}. The glass transition temperature (T_g) values was determined from the onset, while the decomposition temperature (T_{decomp}) was determined from the intersection of the baseline and the tangent of the weight *vs.* temperature, using the Pyris software.

Electrochemistry

All measurements were carried out using an Autolab PGSTAT302N electrochemical workstation (FRA32 M module). The ionic conductivity was measured with a TSC 70 closed cell from RHD instruments, Germany. In the Microcell HC system, the temperature was controlled through a Peltier element, which enables the temperature to be regulated from −20 to 100 °C. For the electrochemical impedance spectroscopy (EIS) measurements, a two-electrode system with a Pt wire as the working electrode (WE) and a Pt cup as a counter electrode (CE), as well as a sample container, was used with the cell constant determined using a 100 μS cm^{-1} KCl standard solution from Metrohm (K_{cell} = 18.5396 cm^{-1}). The frequency range used was from 0.1 Hz to 1 MHz, and the ionic conductivity was analyzed by fitting the EIS data to the Vogel–Fulcher–Tammann (VFT) equation

$$\sigma = \sigma_0 \exp\left(\frac{-B}{(T - T_0)}\right)$$

where σ_0 is a pre-exponential factor, B is a factor related to the activation energy and T_0 is the ideal glass transition temperature. The activation energy of ionic conductivity is related to B *via* $E_\sigma = B \cdot R$.

Linear sweep voltammetry (LSV) was carried out using a three-electrode system, with a Pt wire as the WE, a Pt cup as the CE, and a Ag wire (coated with AgCl) as a pseudo-reference electrode (RE), and with a scan rate of 1 mV s^{-1}. The electrochemical potentials were recorded with ferrocene as the internal reference.[31] The ESW limits were determined using 0.1 mA cm^{-2} as the cut-off current density.[32]

Furthermore, both cyclic voltammetry (CV) and EIS of the ILs as electrolytes for supercapacitors made using graphite electrodes were carried out. Commercially available graphite-coated copper sheets (Cambridge Energy Solutions, UK) were used as electrodes and a TSC battery cell (RHD instruments, Germany) was employed, where the details can be found in our previous publications.[33,34] CV was performed at different scan rates from 1 mV s^{-1} to 200 mV s^{-1} at several temperatures, and EIS was carried out in the frequency range from 0.01 Hz to 1 MHz. The specific capacitance (C_s [F g^{-1}]) was calculated from CV using:[35]

$$C_s = \frac{\int I \mathrm{d}V}{2mK\Delta V}$$

where $\int I \mathrm{d}V$ is the absolute area under the CV curve (I is the current, in A), m is the mass of one electrode (in g), K is the scan rate in (V s^{-1}), and ΔV is the potential window (in V).

Using the galvanostatic charge discharge (GCD) data, the specific capacitance was calculated using the following equation:[36,37]

$$C_s = \frac{(i \times \Delta t)}{(m \times \Delta v)}$$

where C_s denotes the capacitance, I is the current density, m is the mass of both electrodes (3.6 mg), and $\Delta t/\Delta V$ denotes the direct slope of the liberation curve, where Δt is the discharge time and ΔV is the potential difference. The energy and power

19816 | *Phys. Chem. Chem. Phys.*, 2023, **25**, 19815–19823

This journal is © the Owner Societies 2023

densities are given by the equations below, where E_D is the energy density, V is the potential window, P_D is the power density, and the discharge time is given by Δt.

$$E_D = \frac{CV^2}{3.6 \times 2}$$

$$P_D = \frac{E_{D \times 3600}}{\Delta t}$$

NMR diffusometry

Pulsed gradient spin echo-nuclear magnetic resonance (PGSE-NMR) measurements were performed using the Bruker Ascend Aeon WB 400 NMR spectrometer. NMR self-diffusion measurements were carried out for ^{1}H (400.21 MHz) using a Diff50 (Bruker) PGSE-NMR probe. The sample was placed in a standard 5 mm glass sample tube and closed with a plastic stopper to avoid air contact. Before measurements, the sample was equilibrated at a specific temperature for 30 min. The diffusional decay (DD) was recorded using the stimulated echo (StE) pulse train. For single-component diffusion, the form of the DD can be described as:[38]

$$A(\tau, \tau_1, g, \delta) \propto \exp\left(-\frac{2\tau}{T_2} - \frac{\tau_1}{T_1}\right) \exp\left(-\gamma^2 \delta^2 g^2 D t_d\right)$$

Here, A is the integral intensity of the NMR signal; τ is the time interval between first and second radiofrequency pulses; τ_1 is the time interval between second and third radiofrequency pulses; γ is the gyromagnetic ratio for ^{1}H; g and δ are, respectively, the amplitude and the duration of the gradient pulse; $t_d = (\Delta - \delta/3)$ is the diffusion time; Δ is the time interval between two identical gradient pulses; and D is the diffusion coefficient. In the measurements, the duration of the 90° pulse was 7 μs, δ was in the range from 1 to 2 ms, τ was in the range of 3–5 ms, and g was varied from 0.06 up to the maximum of the gradient amplitude, 29.73 T m^{-1}. The diffusion time t_d was varied from 4 to 100 ms. The repetition time during accumulation of the signal transients was 3.5 s. Data were recorded at temperatures ranging from 295 to 373 K. The following VFT equation was used to further analyze the diffusion data:

$$D = D_0 \exp\left(\frac{-B}{(T - T_0)}\right)$$

where T_0 and B are adjustable parameters. The activation energy for diffusion is related to B via $E_D = B \cdot R$.
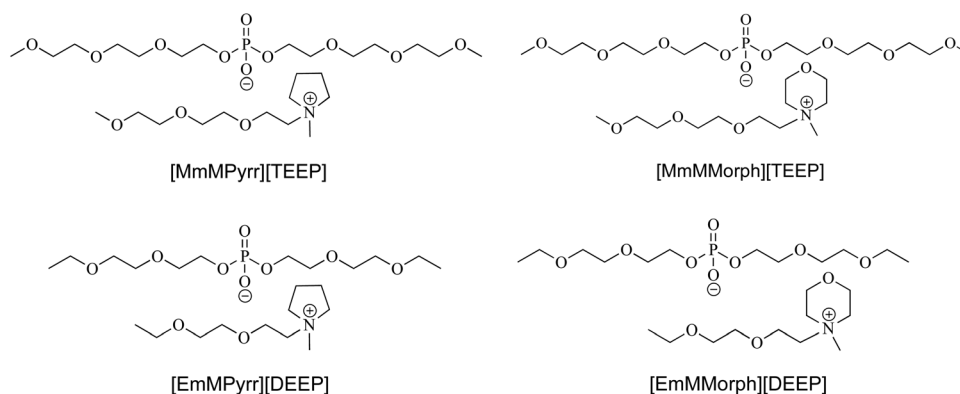
Results and discussion

First, a brief description of the synthesis and structural characterization of the ILs is given, followed by the thermal behaviour, ionic conductivity, ion diffusivity and electrochemical assessment data. Finally, the ion–ion interactions and their role in ion transport and dynamics are described and discussed using both the NMR and FTIR spectroscopy data.

Synthesis and characterization

Following the TMOP and TEOP synthesis (Scheme S1, ESI†),[39] the first set of Pyrr- and Morph-based ILs was synthesized efficiently using single-step reactions between TMOP and either 1-methylpyrrolidine or 4-methylmorpholine in a 1:1 stoichiometric ratio. The corresponding [MmMPyrr][TEEP] and [MmMMorph][TEEP] ILs were obtained in quantitative yields (Scheme S2, ESI†). To investigate the effect of the ion size, [EmMPyrr][DEEP] and [EmMMorph][DEEP], i.e., ILs with shorter oligoether chains on the anions and cations, were prepared using the same procedure (Scheme S3, ESI†). The chemical structures and abbreviations of the synthesized ILs are shown in Scheme 1. In the ^{1}H NMR spectrum of [MmMPyrr][TEEP], the sharp singlet at 3.25 ppm is assigned to the methyl protons attached to the nitrogen atom of the Pyrr ring. The other two different sets of ^{1}H resonance lines observed in the ranges of 3.80–3.76 ppm and 2.25–2.16 ppm correspond to the methylene protons of the Pyrr ring in [MmMPyrr][TEEP]. The ^{1}H resonance lines in the ranges of 3.97–3.82 ppm, 3.63–3.59 ppm and 3.52–3.50 ppm are due to the ethoxy protons, and those in the range of 3.36–3.32 ppm are due to the methoxy protons. All the characteristic ^{13}C resonance lines are observed in the ^{13}C{^{1}H} NMR spectra of all the synthesized ILs. The ^{31}P{^{1}H} NMR spectra of these ILs reveal sharp single resonance lines for the phosphorus nuclei present in the anions. All the ^{1}H, ^{13}C and ^{31}P NMR spectra are presented in the ESI.†

Thermal properties

The TGA data show that the Pyrr-based ILs exhibit 10–15 °C higher decomposition temperatures compared with the

Scheme 1 Chemical structures and abbreviations of the ionic components for the ILs.

This journal is © the Owner Societies 2023

Phys. Chem. Chem. Phys., 2023, **25**, 19815–19823 | **19817**

Morph-based ILs (Fig. 1a and Table 1), while there are no significant differences upon changing the length of the oligoether chain. Differential thermogravimetric (DTG) analysis (Fig. 1b) shows the highest rate of weight loss in a single step for the Pyrr-based ILs, while the maximal rate is reached in two steps for the Morph-based ILs, where > 20 wt% min^{-1} is observed from 270 to 320 $^{\circ}$C. Overall, the thermal stabilities are comparable to/or better than other Pyrr- and Morph-based ILs.[40–42]

The DSC data reveal that all the ILs are glass-forming liquids with glass transition temperature (T_g) values in the range from -59 to -80 $^{\circ}$C (Fig. 2). The Pyrr-based ILs show lower T_g values than the Morph-based ILs, pointing towards weaker cation–anion interactions, and there is weak effect of the oligoether chain length, where the ILs with the longer oligoether chains, *i.e.*, [MmPyrr][TEEP] and [MmMorph][TEEP], exhibit higher glass transition temperatures (Fig. 2 and Table 1), which possibly indicates a more effective packing of the longer oligoether chains.

Ionic conductivity

The ionic conductivities of the Pyrr-based ILs are between around half and one order of magnitude higher than those of the Morph-based ILs (Fig. 3); this may be due to the Morph cations being somewhat bulkier and having stronger ion–ion interactions,[15] including the role of the ring oxygen atom making them more polar, which is also manifested in the higher glass transition temperatures.

The VFT fit parameters (Table S1, ESI†) show that the activation energies for the Morph-based ILs are slightly higher than for the Pyrr-based ILs, and likewise for the [DEEP]$^-$- and [TEEP]$^-$-based ILs, which corroborates well with the DSC data. The ideal glass transition temperatures (T_o) are 50–60 K lower than the measured glass transition temperatures (T_g), which is in accordance with the common empirical approximation for ILs (and other liquids).[43]

NMR diffusometry

The PFG NMR diffusion data reveal a continuous increase in the diffusivity of all ions as a function of increasing temperature, which follows the VFT behavior (Fig. 4 and Table S2, ESI†). Both ions in the [MmPyrr][TEEP] IL diffuse faster than those in the [EmPyrr][DEEP] IL, thus indicating that ion–ion interactions
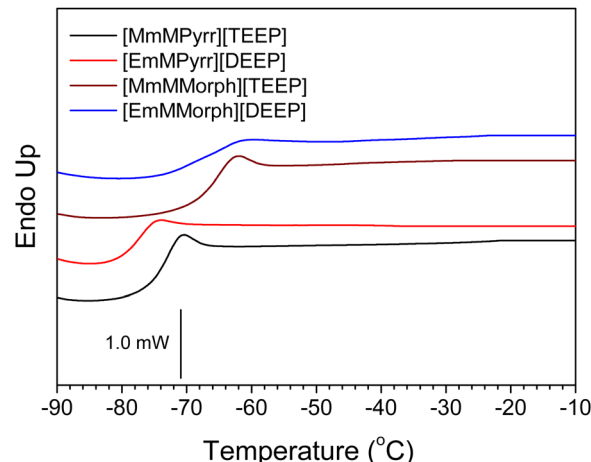

Fig. 2 DSC traces of the Pyrr- and Morph-based ILs.
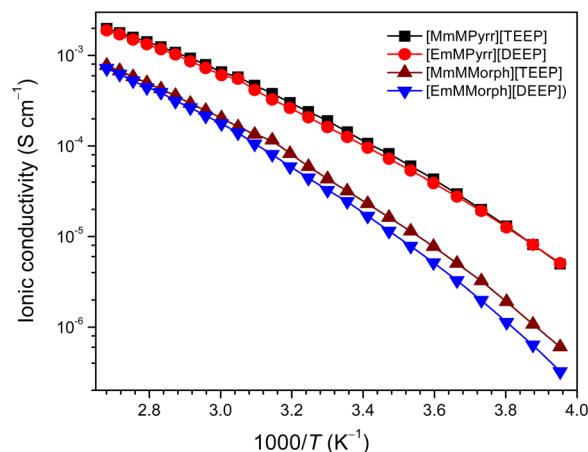

Fig. 3 Ionic conductivities of the Pyrr- and Morph-based ILs. The symbols denote the experimental data and the solid lines show the best fit to the VFT equation for each.

are more important than the ion sizes – as also observed previously for other ILs[44] – and that the stronger positive resonance or mesomeric effect of the ethoxy groups in both the [EmPyrr]$^+$ cation and the [DEEP]$^-$ anion stabilizes both.
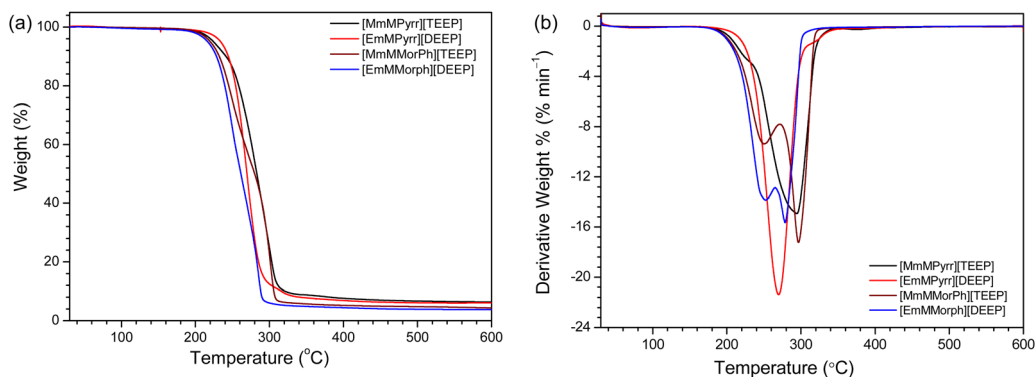

Fig. 1 (a) TGA thermograms and (b) DTG curves of the Pyrr- and Morph-based ILs.

19818 | *Phys. Chem. Chem. Phys.*, 2023, **25**, 19815–19823

This journal is © the Owner Societies 2023

In stark contrast to the Pyrr-based ILs, both the cation and the anion in the [EmMMorph][DEEP] IL diffuse faster than the corresponding ions in the [MmMMorph][TEEP] IL. Overall, the ion mobility in the Pyrr-based ILs is significantly higher than in the Morph-based ILs, primarily due to the smaller cation sizes and (presumably, see below) weaker ion–ion interactions, as shown by the D_0 value being more than twice as large, whilst at the same time showing rather similar molar activation energies (Table S2, ESI†).

Electrochemistry

Starting with the anodic stabilities, the ILs are stable up to +3.32 V *vs.* Fc/Fc$^+$, while the cathodic limits are close to −1.75 V *vs.* Fc/Fc$^+$ (Fig. 5, and Table S3, ESI†). We stress that our set cut-off current density is 0.1 mA cm^{-2} and thus all the ESWs are very conservative.[45] Overall, the ESWs of these ILs are ∼4.5 V, with the [MmMMorph][TEEP] IL being the most stable (>5.0 V), which is wider compared with previously reported Pyrr- and Morph-based ILs.[46,47] After establishing the electrochemical stability, the [EmMPyrr][DEEP] and [EmMMorph][DEEP] ILs were further evaluated as electrolytes in symmetric graphite supercapacitors (SCs).

Moving to the evaluation of these ILs as electrolytes in SCs, the [EmMPyrr][DEEP] IL shows a much better performance compared with the [EmMMorph][DEEP] IL (Fig. 6 and Fig. S23 (ESI†)), which can simply be attributed to its higher ionic conductivity and ion diffusivity. At a device level, the specific capacitance decreases with increasing scan rate whereas it increases as a function of temperature (Fig. S24 and S25, ESI†), where the latter is enabled by the thermal stability of the ILs and improved ion–ion dissociation and mobility. Overall, the Pyrr-based IL shows typical capacitive behaviour, with a uniform current–potential fluctuation and no CV plot distortion, while a modest distortion and poor capacitive performance is observed for the Morph-based IL, suggesting worse wetting of the electrode pores.[48]
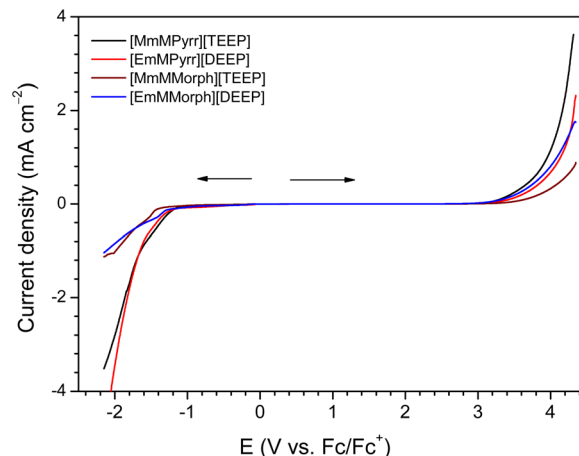

Fig. 5 Cathodic and anodic LSV scans of the Pyrr- and Morph-based ILs.

That the SC with [EmMPyrr][DEEP] IL as an electrolyte has both a higher specific capacitance and reversibility at elevated temperatures is due primarily to this IL's higher ionic conductivity and lower resistivity, as confirmed by the EIS data (Fig. S26, ESI†). Both ILs exhibit straight lines in the lower frequency domain, and hence capacitive behaviour,[49] while their redox behaviour leads to uneven semicircles.[50] In terms of the performance, the SC with the [EmMPyrr][DEEP] IL as an electrolyte rendered a specific energy density of ∼27 W h kg^{-1} and a power density of ∼609 W kg^{-1} at a current density of 0.5 A g^{-1}. By comparison, the SC with the Morph-based IL as an electrolyte exhibited around a ten-fold lower energy density, but a comparable power density (Fig. S27 and Table S4, ESI†). However, both the ILs showed a similar cyclic stability and capacitance retention up to 150 cycles at a current density of 1.5 A g^{-1} (Fig. S28, ESI†).

The capacitance of a supercapacitor is greatly influenced by the ion diffusion in the bulk as well as inside the porous electrodes. A faster ion diffusion facilitates faster charging and discharging processes.[51] Due to their smaller cation size, Pyrr-based ILs improve the specific capacitance and show a lower resistance than conventional imidazolium- and pyridinium-based ILs for the same anion, which mechanistically is attributed to an increased ion concentration in the double-layer.[52] The nature of the anion also plays a crucial role; the [Pyr$_{1,4}$][C(CN)$_3$] IL shows a much better performance than the analogous IL based on the [TFSI]$^-$ anion, especially at higher C-rates.[53] Similarly, the [EmMPyrr][DEEP] IL outperforms the [EmMMorph][DEEP] IL due to the faster ion diffusion and higher ion conductivity.

NMR and FTIR spectroscopy

The ^{31}P NMR resonance lines are broader at lower temperatures and become sharper as a function of temperature (Fig. 7a), suggesting faster re-orientational dynamics,[54] and in the case of the Morph-based ILs this is also due to ion–ion dissociation, which is supported by the observed chemical shifts as a function of temperature that also suggest decreased interactions between the anions and the corresponding cations (Fig. 7b and Fig. S29, ESI†).

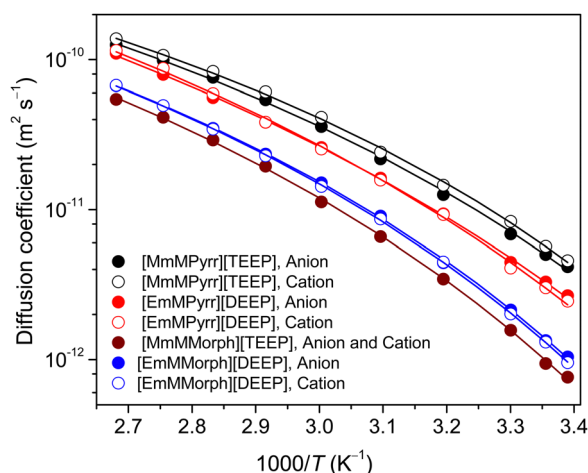Turning to the FTIR spectroscopy data, all the characteristic stretching frequencies for the functional groups of the

Fig. 4 Ion diffusion coefficients for the ions in the Pyrr- and Morph-based ILs. The symbols denote the experimental data and the solid lines show the best fit to the VFT equation for each.
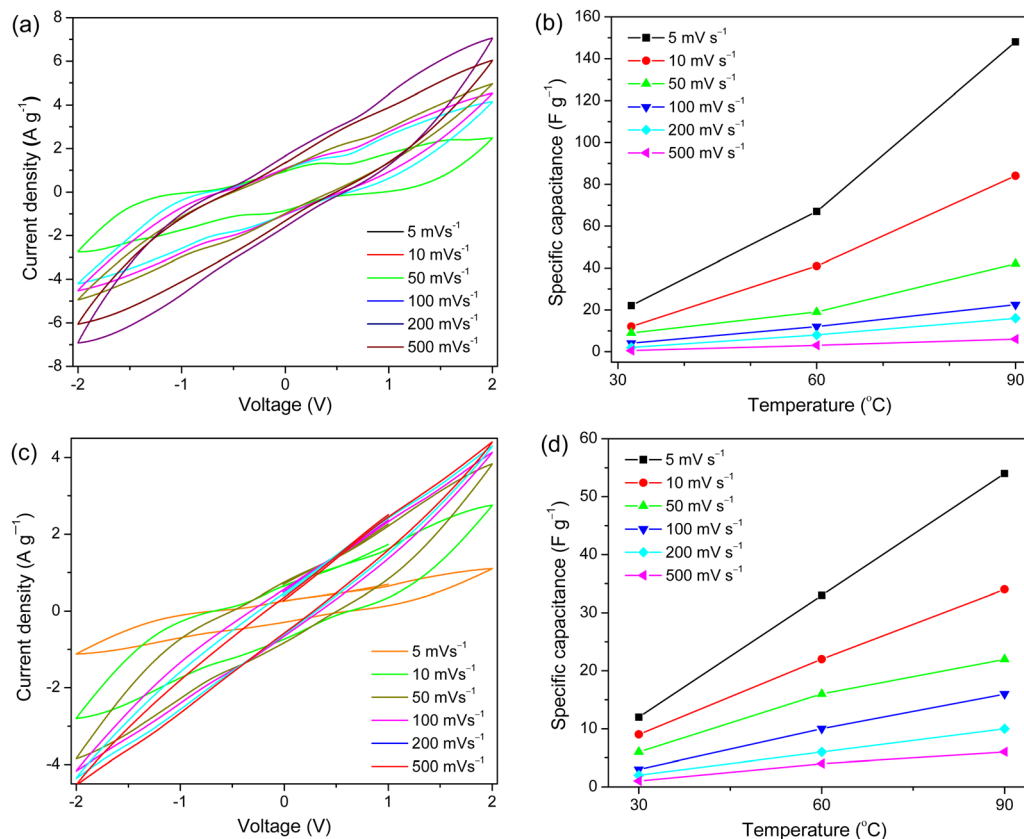
Fig. 6 Cyclic voltammograms obtained using different scan rates at 90 °C (a) and (c) and the specific capacitance as a function of temperature (b) and (d) for SCs made using the [EmMPyrr][DEEP] IL (a and b) and [EmMMorph][DEEP] IL electrolytes (c and d).

neutral TMOP and TEOP compounds, such as P=O, PO_3, O–P–O and P–O–C, are shifted, which confirms the formation of the [TEEP]⁻ and [DEEP]⁻ anions in the Pyrr- and Morph-based ILs (Fig. 8).[55] The symmetric P=O stretching band shifts to a lower wavenumber ($\sim$1250 cm⁻¹) for both [MmMPyrr][TEEP] and [MmMMorph][TEEP], and to $\sim$1255 cm⁻¹ for [EmMPyrr][DEEP] and [EmMMorph][DEEP] (Fig. 8a and c). The PO_3 stretching band shifts to a higher wavenumber ($\sim$1066 cm⁻¹) for all ILs, while the O–P–O stretching band shifts towards a lower wavenumber ($\sim$950 cm⁻¹;

Fig. 8c and d) due to the formation of anions from the neutral TMOP and TEOP compounds. Overall, larger shifts are observed for the Morph-based ILs than for the Pyrr-based ILs, suggesting stronger ion–ion interactions. In addition, some prominent changes are observed between 700 and 800 cm⁻¹, *i.e.*, the (P–O)–C stretching band, where the band around 775–780 cm⁻¹ in the spectra of the Morph-based ILs is shifted down for the Pyrr-based ILs, again clearly indicating that the Morph-based ILs have stronger ion–ion interactions.
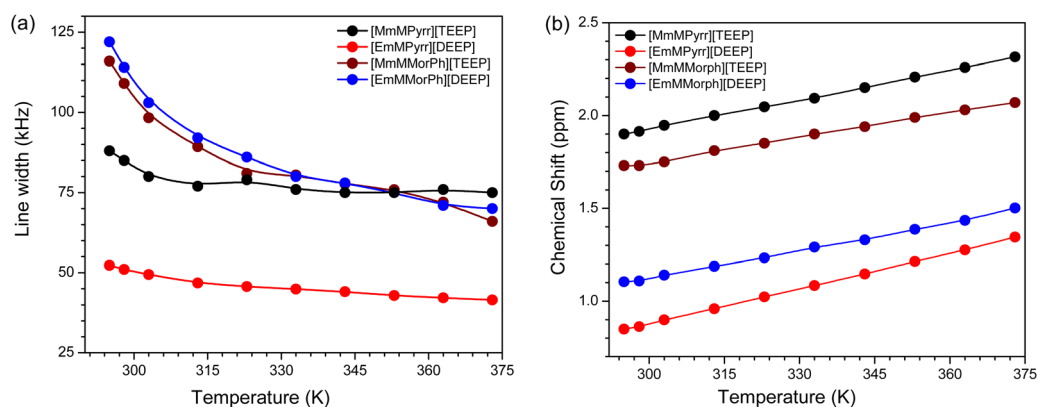

Fig. 7 (a) ³¹P NMR spectral line widths and (b) ³¹P NMR chemical shifts of the ILs as a function of temperature.

19820 | *Phys. Chem. Chem. Phys.*, 2023, **25**, 19815–19823
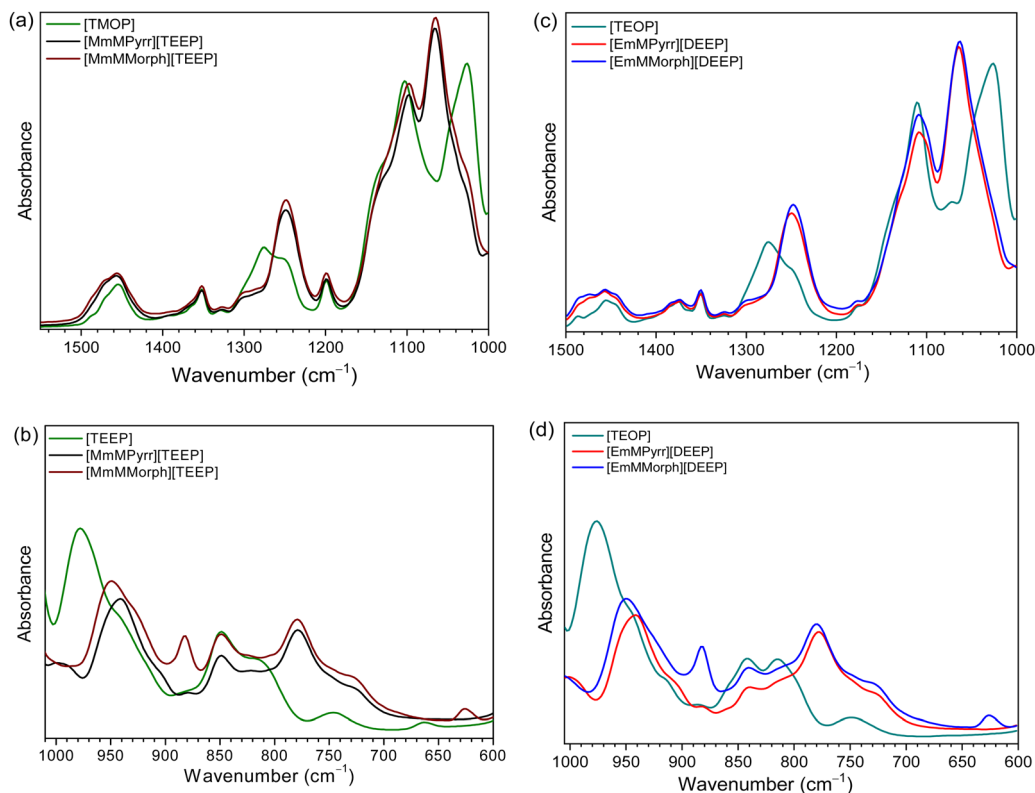
This journal is © the Owner Societies 2023

Fig. 8 FTIR spectra of the neutral compounds and the ILs in the frequency range of 600–1500 cm^{-1}.

Conclusions

The new Pyrr-based ILs exhibited favourable properties compared with the structurally analogous Morph-based ILs that bear common oligoether phosphate anions. Despite their comparable molecular masses and ion sizes, the Pyrr-based ILs displayed higher thermal stabilities and better transport properties over a wide temperature range than did the corresponding Morph-based ILs. The rapid ion dissociation as a function of temperature, particularly for the Morph-based ILs, is a result of weaker cation–anion interactions, as confirmed *via* both FTIR and NMR spectroscopy. Having superior transport properties, the Pyrr-based ILs performed much better as electrolytes in supercapacitors, particularly at elevated temperatures. Altogether, this study confirmed that the Pyrr-based ILs offered more beneficial properties than the structurally similar Morph-based ILs, suggesting that the Pyrr-based ILs can potentially be used as electrolytes in energy storage devices.

Conflicts of interest

There are no conflicts to declare.

Acknowledgements

References

1 R. D. Rogers and K. R. Seddon, Ionic liquids-solvents of the future?, *Science*, 2003, **302**, 792–793.

2 M. Armand, F. Endres, D. R. MacFarlane, H. Ohno and B. Scrosati, Ionic-liquid materials for the electrochemical challenges of the future, *Nat. Mater.*, 2009, **8**, 621–629.

3 J. P. Hallett and T. Welton, Room-temperature ionic liquids: solvents for synthesis and catalysis, *Chem. Rev.*, 2011, **111**, 3508–3576.

4 F. U. Shah, S. Glavatskih, D. R. MacFarlane, A. Somers, M. Forsyth and O. A. Antzutkin, Novel halogen-free chelated orthoborate-phosphonium ionic liquids: synthesis and tribophysical properties, *Phys. Chem. Chem. Phys.*, 2011, **13**, 12865–12873.

5 F. U. Shah, S. Glavatskih, P. M. Dean, D. R. MacFarlane, M. Forsyth and O. N. Antzutkin, Halogen-free chelated orthoborate ionic liquids and organic ionic plastic crystals, *J. Mater. Chem.*, 2012, **22**, 6928–6938.

6 S. Bhattacharyya, A. Filippov and F. U. Shah, Insights into the effect of CO$_2$ absorption on the ionic mobility of ionic liquids, *Phys. Chem. Chem. Phys.*, 2016, **18**, 28617–28625.

7 O. Nacham, K. D. Clark, H. L. Yu and J. L. Anderson, Synthetic strategies for tailoring the physicochemical and

magnetic properties of hydrophobic magnetic ionic liquids, *Chem. Mater.*, 2015, **27**, 923–931.

8 L. He, S. P. Ji, N. Tang, Y. Zhao and G. H. Tao, Synthesis, structure and near-infrared photoluminescence of hexanitratoneodymate ionic liquids, *Dalton Trans.*, 2015, **44**, 2325–2332.

9 M. R. Shimpi, S. P. Velaga, F. U. Shah and O. N. Antzutkin, Pharmaceutical crystal engineering using ionic liquid anion-solute interactions, *Cryst. Growth Des.*, 2017, **17**, 1729–1734.

10 N. Nikfarjam, M. Ghomi, T. Agarwal, M. Hassanpour, E. Sharifi, D. Khorsandi, M. A. Khan, F. Rossi, A. Rossetti, E. N. Zare, N. Rabiee, D. Afshar, M. Vosough, T. K. Maiti, V. Mattoli, E. Lichtfouse, F. R. Tay and P. Makvandi, Antimicrobial ionic liquid-based materials for biomedical applications, *Adv. Funct. Mater.*, 2021, **31**, 2104148.

11 S. Beil, M. Markiewicz, C. S. Pereira, P. Stepnowski, J. Thöming and S. Stolte, Toward the Proactive Design of Sustainable Chemicals: Ionic Liquids as a Prime Example, *Chem. Rev.*, 2021, **121**, 13132–13173.

12 Y. O. Andriyko, W. Reischl and G. E. Nauer, Trialkylsubstituted imidazolium-based ionic liquids for electrochemical applications: basic physicochemical properties, *J. Chem. Eng. Data*, 2009, **54**, 855–860.

13 A. Zajac, A. Szpecht, A. Szymanska, D. Zielinski, O. Stolarska, M. Smiglak and H. Maciejewski, Synthesis and characterization of nitrogen-based ionic liquids bearing allyl groups and examples of their application, *New J. Chem.*, 2020, **44**, 12274–12288.

14 T. N. Barrett, J. A. Tylor, D. Barker, P. A. Procopiou, J. D. F. Thompson, J. Barrett, J. Le, S. M. Lynn, P. Pogany, C. Pratley, J. M. Pritchard, J. A. Roper, J. E. Rowedder, R. J. Slack, G. Vitulli, S. J. F. Macdonald and W. J. Kerr, Profile of a Highly Selective Quaternized Pyrrolidine Betaine αvβ6 Integrin Inhibitor (3*S*)-3-(3-(3,5-Dimethyl-1*H*-pyrazol-1-yl)phenyl)-4-((1*S* and 1*R*,3*R*)-1-methyl-3-(2-(5,6,7,8-tetrahydro-1,8- naphthyridin-2-yl)ethyl)Pyrrolidin-1-ium-1-yl)butanoate Synthesized by Stereoselective Methylation, *J. Med. Chem.*, 2019, **62**, 7543–7556.

15 S. H. Yeon, K. S. Kim, S. Choi, H. Lee, H. S. Kim and H. Kim, Physical and electrochemical properties of 1-(2-hydroxyethyl)-3-methyl imidazolium and *N*-(2-hydroxyethyl)-*N*-methyl Morpholinium ionic liquids, *Electrochim. Acta*, 2005, **50**, 5399–5407.

16 S. Ferrari, E. Quartarone, P. Mustarelli, A. Magistris, M. Fagnoni, S. Protti, C. Gerbaldi and A. Spinella, Lithium ion conducting PVdFHFP composite gel electrolytes based on *N*-methoxyethyl-NmethylPyrrolidinium bis(trifluoromethanesulfonyl)-imide ionic liquid, *J. Power Sources*, 2010, **195**, 559–566.

17 C. Samorì, T. Campisi, M. Fagnoni, P. Galletti, A. Pasteris, L. Pezzolesi, S. Protti, D. Ravelli and E. Tagliavini, Pyrrolidinium-based Ionic Liquids: Aquatic Ecotoxicity, Biodegradability, and Algal Subinhibitory Stimulation, *ACS Sustainable Chem. Eng.*, 2015, **3**, 1860–1865.

18 R. S. P. Fonseca1, F. C. Silva, F. S. M. Sinfrônio, C. D. J. S. Mendonça and I. S. D. S. Neto, Synthesis of Morpholine-Based Ionic Liquids for Extractive Desulfurization of Diesel Fuel, *Braz. J. Chem. Eng.*, 2019, **36**, 1019–1027.

19 J. Neumann, S. Steudte, C.-W. Cho, J. Thöming and S. Stolte, Biodegradability of 27 Pyrrolidinium, Morpholinium, piperidinium, imidazolium and pyridinium ionic liquid cations under aerobic conditions, *Green Chem.*, 2014, **16**, 2174–2184.

20 K. Liu, W. Liu, Y. Qiu, B. Kong, Y. Sun, Z. Chen, D. Zhuo, D. Lin and Y. Cui, Electrospun core-shell microfber separator with thermaltriggered fame-retardant properties for lithium-ion batteries, *Sci. Adv.*, 2017, **3**, e1601978.

21 Y.-K. Sun, Z. Chen, H.-J. Noh, D.-J. Lee, H.-G. Jung, Y. Ren, S. Wang, C.-S. Yoon, S.-T. Myung and K. Amine, Nanostructured high-energy cathode materials for advanced lithium batteries, *Nat. Mater.*, 2012, **11**, 942.

22 M. Q. Xu, L. D. Xing, W. S. Li, X. X. Zuo, D. Shu and G. L. Li, Application of cyclohexyl benzene as electrolyte additive for overcharge protection of lithium ion battery, *J. Power Sources*, 2008, **184**, 427–431.

23 W. Weng, J. Huang, I. A. Shkrob, L. Zhang and Z. Zhang, Redox shuttles with axisymmetric scafold for overcharge protection of lithium-ion batteries, *Adv. Energy Mater.*, 2016, **6**, 1600795.

24 E. Mendelsohn, A. Hagopian, K. Hoffman, C. M. Butt, A. Lorenzo, J. Congleton, T. F. Webster and H. M. Stapleton, Nail polish as a source of exposure to triphenyl phosphate, *Environ. Int.*, 2016, **86**, 45–51.

25 K. Xu, S. S. Zhang, J. L. Allen and T. R. Jow, Nonflammable Electrolytes for Li-Ion Batteries Based on a Fluorinated Phosphate, *J. Electrochem. Soc.*, 2002, **149**, A1079.

26 X. M. Wang, E. Yasukawa and S. Kasuya, Nonflammable Trimethyl Phosphate Solvent-Containing Electrolytes for Lithium-Ion Batteries: I. Fundamental Properties, *J. Electrochem. Soc.*, 2001, **148**, A1058.

27 Y. E. Hyung, D. R. Vissers and K. Amine, Flame-retardant additives for lithium-ion batteries, *J. Power Sources*, 2003, **119**, 383–387.

28 Z. Zhao, D.-M. Guo, T. Fu, X.-L. Wang and Y.-Z. Wang, A highly-effective ionic liquid flame retardant towards firesafety waterborne polyurethane (WPU) with excellent comprehensive performance, *Polymer*, 2020, **205**, 122780.

29 H. Nakagawa, Y. Fujino, S. Kozono, Y. Katatyama, T. Nukuda, H. Sakaebe, H. Matsumoto and K. Tatsumi, Application of nonflammable electrolyte with room temperature ionic liquids (RTILs) for lithium-ion cells, *J. Power Sources*, 2007, **174**, 1021–1026.

30 C. P. Fredlake, J. M. Crosthwaite, D. G. Hert, S. N. V. K. Aki and J. F. Brennecke, Thermophysical properties of imidazolium-based ionic liquids, *J. Chem. Eng. Data*, 2004, **49**, 954–964.

31 A. R. Neale, S. Murphy, P. Goodrich, C. Hardacre and J. Jacquemin, J. Thermophysical and electrochemical properties of ethereal functionalised cyclic alkylammonium-based ionic liquids as potential electrolytes for electrochemical applications, *Chem. Phys. Chem.*, 2017, **18**, 2040–2057.

32 Z. Xue, L. Qin, J. Jiang, T. Mu and G. Gao, Thermal, electrochemical and radiolytic stabilities of ionic liquids, *Phys. Chem. Chem. Phys.*, 2018, **20**, 8382–8402.

19822 | *Phys. Chem. Chem. Phys.*, 2023, **25**, 19815–19823

This journal is © the Owner Societies 2023

33 I. A. Khan and F. U. Shah, Fluorine-free ionic liquid-based electrolyte for supercapacitors operating at elevated temperatures, *ACS Sustainable Chem. Eng.*, 2020, **27**, 10212–10221.

34 I. A. Khan, Y. L. Wang and F. U. Shah, Effect of structural variation in biomass-derived nonfluorinated ionic liquids electrolytes on the performance of supercapacitors, *J. Energy Chem.*, 2022, **69**, 174–184.

35 G. Tatrari, C. Tewari, M. Pathak, M. Karakoti, B. S. Bohra, S. Pandey, B. S. Bhushan, A. Srivastava, S. Rana and N. G. Sahoo, Bulk production of zinc doped reduced graphene oxide from tire waste for supercapacitor application: computation and experimental analysis, *J. Energy Storage*, 2022, **53**, 105098.

36 S. Zhang and N. Pan, Supercapacitors performance evaluation, *Adv. Energy Mater.*, 2015, **5**, 1401401.

37 J. Zhao and A. F. Burke, Review on supercapacitors: Technologies and performance evaluation, *J. Energy Chem.*, 2021, **59**, 276–291.

38 T. E. Tanner, Use of the stimulated echo in NMR diffusion studies, *J. Chem. Phys.*, 1970, **52**, 2523–2526.

39 S. Bhowmick, M. Ahmed, A. Filippov, L. C. Loaiza, F. U. Shah and P. Johansson, Ambient temperature liquid salt electrolytes, *Chem. Commun.*, 2023, **59**, 2620–2623.

40 J. M. Fischer, P. Do, R. M. Reich, A. Nagasubramanian, M. Srinivasan and F. E. Kuhn, Synthesis and physicochemical characterization of room temperature ionic liquids and their application in sodium ion batteries, *Phys. Chem. Chem. Phys.*, 2018, **20**, 29412–29422.

41 A. J. Ward, A. F. Masters and T. Maschmeyer, Facile, high-yielding preparation of Pyrrolidinium, piperidinium, Morpholinium and 2,3-dihydro-1Hisoindolinium salts and ionic liquids from secondary amines, *RSC Adv.*, 2014, **4**, 23327–23337.

42 B. Gorska, L. Timperman, M. Anouti, J. Pernaka and F. Beguin, F. Physicochemical and electrochemical properties of a new series of protic ionic liquids with Nchloroalkyl functionalized cations, *RSC Adv.*, 2016, **6**, 55144–55158.

43 M. Galinski, A. Lewandowski and I. Stepniak, Ionic Liquids as Electrolytes, *Electrochim. Acta*, 2006, **51**, 5567–5580.

44 S. Tsuzuki, Factors Controlling the Diffusion of Ions in Ionic Liquids, *Chem. Phys. Chem.*, 2012, **13**, 1–8.

45 A. M. O'Mahony, D. S. Silvester, L. Aldous, C. Hardacre and R. G. Compton, Effect of water on the electrochemical window and potential limits of room-temperature ionic liquids, *J. Chem. Eng. Data*, 2008, **53**, 2884–2891.

46 C. Brigouleix, M. Anouti, J. Jacquemin, M. Caillon-Caravanier, H. Galiano and D. Lemordant, Physicochemical Characterization of Morpholinium Cation Based Protic Ionic Liquids Used As Electrolytes, *J. Phys. Chem. B*, 2010, **114**, 1757–1766.

47 S. Asha, K. P. Vijayalakshmi and B. K. George, Pyrrolidinium-based ionic liquids as electrolytes for lithium batteries: A Computational Study, *Int. J. Quantum Chem.*, 2019, **119**, e26014.

48 G. Tatrari, M. Karakoti, C. Tewari, S. Pandey, B. S. Bohra, A. Dandapat and N. G. Sahoo, Solid waste-derived carbon nanomaterials for supercapacitor applications: a recent overview, *Mater. Adv.*, 2021, **2**, 1454–1484.

49 B. A. Mei, O. Munteshari, J. Lau, B. Dunn and L. Pilon, Physical interpretations of Nyquist plots for EDLC electrodes and devices, *J. Phys. Chem. C*, 2018, **122**, 194–206.

50 H. C. Huang, C. W. Huang, C. T. Hsieh and H. Teng, Electric double layer capacitors of high volumetric energy based on ionic liquids and hierarchical-pore carbon, *J. Mater. Chem. A*, 2014, **2**, 14963–14972.

51 A. C. Forse, J. M. Griffin, C. Merlet, P. M. Bayley, H. Wang, P. Simon and C. P. Grey, NMR Study of ion dynamics and charge storage in ionic liquid supercapacitors, *J. Am. Chem. Soc.*, 2015, **137**, 7231–7242.

52 A. J. R. Rennie, N. Sanchez-Ramirez, R. M. Torresi and P. J. Hall, Ether-bond-containing ionic liquids as supercapacitor electrolytes, *J. Phys. Chem. Lett.*, 2013, **4**, 2970–2974.

53 V. L. Martins, A. J. R. Rennie, R. M. Torresi and P. J. Hall, Ionic liquids containing tricyanomethanide anions: physicochemical characterisation and performance as electrochemical double-layer capacitor electrolytes, *Phys. Chem. Chem. Phys.*, 2017, **19**, 16867–16874.

54 R. Nanda and K. Damodaran, A review of NMR methods used in the study of the structure and dynamics of ionic liquids, *Magn. Reson. Chem.*, 2018, **56**, 62–72.

55 S. Bhowmick, A. Filippov, I. A. Khan and F. U. Shah, Physical and electrochemical properties of new structurally flexible imidazolium phosphate ionic liquids, *Phys. Chem. Chem. Phys.*, 2022, **24**, 23289–23300.

This journal is © the Owner Societies 2023

Phys. Chem. Chem. Phys., 2023, **25**, 19815–19823 | **19823**